ATLAS NOTE

ATLAS-CONF-2012-165

December 4, 2012

Search for direct sbottom pair production in events with missing transverse momentum and two b-jets in 12.8 fb^{-1} of pp collisions at $\sqrt{s}$ = 8 TeV with the ATLAS detector

The ATLAS Collaboration

Abstract

A search for direct pair production of bottom squarks, each decaying into a bottom quark and a neutralino, is performed in events with large missing transverse momentum and 2 b-jets in the final state using 12.8 fb^{-1} of pp collisions at $\sqrt{s} = 8$ TeV recorded by the ATLAS detector at the LHC. For the particular scenario considered, sbottom masses up to 620 GeV are excluded for neutralino masses below 150 GeV. Differences in mass above 40 GeV between the $\tilde{b}_1$ and the $\tilde{\chi}_1^0$ are excluded up to sbottom masses of 300 GeV. Neutralino masses are also excluded up to 320 GeV for sbottom masses around 550 GeV.

1 Introduction

Supersymmetry (SUSY) [1–9] provides an extension of the Standard Model (SM) which resolves the hierarchy problem [10–13] by introducing supersymmetric partners of the known bosons and fermions. In the framework of the R-parity conserving minimal supersymmetric extension of the SM (MSSM) [14–18], SUSY particles are produced in pairs and the lightest supersymmetric particle (LSP) is stable, providing a possible candidate for dark matter. In a large variety of models, the LSP is the lightest neutralino ($\tilde{\chi}_1^0$). The coloured superpartners of quarks and gluons, the squarks ($\tilde{q}$) and gluinos ($\tilde{g}$), if not too heavy, would be produced in strong interaction processes at the Large Hadron Collider (LHC) and decay via cascades ending with the LSP. The undetected LSP results in missing transverse momentum – whose magnitude is referred to as $E_{\mathrm{T}}^{\mathrm{miss}}$ – while the rest of the cascade yields final states with multiple jets and possibly leptons. In the MSSM, the large value of the top quark Yukawa coupling tends to drive the mass of the superpartners of the third generation quarks to values lower than those of the first and second generation squarks. This effect is enhanced by mixing effects which are proportional to the mass of the SM partner. As a consequence, $\tilde{b}_1$ and $\tilde{t}_1$ (the lightest mass eigenstates of the sbottom and stop particles) could be produced with relatively large cross-sections at the LHC, either directly in pairs, or through $\tilde{g}\tilde{g}$ production followed by $\tilde{g} \to \tilde{b}_1 b$ or $\tilde{g} \to \tilde{t}_1 t$ decays.

The present analysis considers a dataset of 12.8 fb^{-1} collected in 2012 at a centre-of-mass energy of 8 TeV and extends the searches for direct $\tilde{b}_1$ pair production at ATLAS reported earlier [19,20], which used up to 4.7 fb^{-1} of data collected in 2011 at a centre-of-mass energy of 7 TeV. It is based on a similar event selection, requiring large $E_{\mathrm{T}}^{\mathrm{miss}}$, no electrons or muons and two jets identified as originating from b-quarks (b-jets) in the final state. Results are interpreted in a simplified model where sbottoms are produced in pairs and each decays exclusively to a bottom quark and a stable neutralino.

2 The ATLAS detector

The ATLAS detector [21] consists of inner tracking devices surrounded by a superconducting solenoid, electromagnetic and hadronic calorimeters and a muon spectrometer with a toroidal magnetic field. The inner detector, in combination with the 2 T field from the solenoid, provides precision tracking of charged particles for $|\eta| < 2.5$[1]. It consists of a silicon pixel detector, a silicon strip detector and a straw tube tracker that also provides transition radiation measurements for electron identification. The calorimeter system covers the pseudorapidity range $|\eta| < 4.9$. It is composed of sampling calorimeters with either liquid argon (LAr) or scintillating tiles as the active medium. The muon spectrometer has separate trigger and high-precision tracking chambers which provide muon identification and momentum measurement for $|\eta| < 2.7$.

3 Monte Carlo simulation

Samples of simulated events are used for the description of the background and to model the SUSY signal. The dominant sources of background come from events in which b-quarks are produced. Monte Carlo (MC) samples of $t\bar{t}$ events are generated using POWHEG [22] interfaced

[1] ATLAS uses a right-handed coordinate system with its origin at the nominal interaction point (IP) in the centre of the detector and the z-axis along the beam pipe. The x-axis points from the IP to the centre of the LHC ring, and the y axis points upward. Cylindrical coordinates (r, ϕ) are used in the transverse plane, ϕ being the azimuthal angle around the beam pipe. The pseudorapidity is defined in terms of the polar angle θ as $\eta = -\ln\tan(\theta/2)$. The distance ΔR in the $\eta - \phi$ space is defined as $\Delta R = \sqrt{(\Delta\eta)^2 + (\Delta\phi)^2}$.

to PYTHIA [23] and the next-to-leading order (NLO) parton distribution function (PDF) set CT10 [24]. Single top production is generated using AcerMC [25] interfaced to PYTHIA and the PDF set CTEQ6L1 [26] for the t-channel and using MC@NLO [27] interfaced to HERWIG [28] and JIMMY [29] for the s-channel and Wt processes. The W and Z bosons produced in association with light- (u,d,s) and heavy- (c,b) flavoured jets are generated with SHERPA [30] and the PDF set CT10. Diboson events are generated with up to three additional partons using SHERPA [30] and the PDF set CT10. Samples of $t\bar{t}$+W, $t\bar{t}$+Z events are generated with MADGRAPH [31] interfaced to PYTHIA [23] and the PDF set CTEQ6L1. The SUSY signal samples are generated using MADGRAPH interfaced to Pythia 6 in order to ensure an accurate treatment of the initial-state radiation (ISR), using the PDF set CTEQ6L1. The MC samples are processed through the ATLAS detector simulation [32] taking into account the effect of multiple pp interactions per bunch crossing. For comparison with data, all SM background cross-sections are normalised to the results of higher-order calculations.

4 Object reconstruction

Jets are reconstructed from three-dimensional calorimeter energy clusters using the anti-k_t jet algorithm [33,34] with a radius parameter of 0.4. The measured jet energy is corrected for inhomogeneities and for the non-compensating nature of the calorimeter by weighting differently energy deposits arising from electromagnetic and hadronic showers using correction factors derived from Monte Carlo simulations and validated with data [35]. An additional calibration is subsequently applied to the corrected jet energies relating the response of the calorimeter to the true jet energy. The impact of additional collisions in the same or neighbouring bunch crossings is also taken into account using offset corrections derived as a function of the average number of interactions per event $\langle\mu\rangle$ and of the number of primary vertices N_{PV} [35]. Jets are required to have transverse momentum (p_{T})$>$ 20 GeV, and are reconstructed in the range $|\eta| < 4.9$. Events are rejected if they include jets failing the quality criteria described in Ref. [35]. To further reject spurious jet signals originating from cosmic rays or detector malfunctioning, additional criteria are applied on the charged p_{T} fraction chf, defined as the ratio between the sum of the p_{T} of all tracks associated to the jet and the jet p_{T}, and on the fraction of the jet energy contained in the electromagnetic layers of the calorimeter emf. Events are rejected if any of the two leading jets with $p_T > 100$ GeV and $|\eta| < 2.0$ satisfies either $chf < 0.02$ or both $chf < 0.05$ and $emf > 0.9$. A neural-network-based algorithm [36] is used to identify jets containing a b-hadron decay. This uses as inputs the output weights of different algorithms exploiting the impact parameter of the inner detector tracks, the secondary vertex reconstruction and the topology of b- and c-hadron decays inside the jet. The algorithm used has an efficiency of 60% for tagging b-jets in a MC sample of $t\bar{t}$ events and a rejection of 580, 8 and 23 against light quarks, c-quarks and τ leptons respectively. The b-jets are identified within the nominal acceptance of the inner detector ($|\eta| < 2.5$) and are required to have $p_{\mathrm{T}} > 20$ GeV.

Electrons are reconstructed from energy clusters in the electromagnetic calorimeter matched to a track in the inner detector. Electron candidates are required to have $p_{\mathrm{T}} > 10$ GeV and $|\eta| < 2.47$ and must satisfy the "medium" selection criteria described in Ref. [37]. Tight electrons, used for the control regions, are selected using "tight" criteria, $p_{\mathrm{T}} > 25$ GeV, and with the isolation requirement that the total track momentum in a cone of $\Delta R < 0.2$ around the candidate be less than 10% of the reconstructed p_{T}. Muon candidates are identified using a match between an extrapolated inner detector track and one or more track segments in the muon spectrometer, and are required to have $p_{\mathrm{T}} > 10$ GeV and $|\eta| < 2.4$. Tight muons are required to have $p_{\mathrm{T}} > 20$ GeV and less than 1.8 GeV in a cone of $\Delta R < 0.2$ around the candidate.

To resolve overlaps between reconstructed jets and leptons, jets within a distance of $\Delta R = 0.2$ of an electron candidate are rejected. Furthermore, any lepton candidate with a distance $\Delta R < 0.4$ to the closest jet is discarded.

The missing transverse momentum, $E_{\mathrm{T}}^{\mathrm{miss}}$, is the magnitude of the vector sum of the transverse momentum or transverse energy of all $p_{\mathrm{T}} > 10$ GeV muons, $E_T > 10$ GeV electrons, $E_T > 20$ GeV jets, and calibrated calorimeter energy clusters with $|\eta| < 4.9$ not associated to these objects. Reconstructed tracks are used to suppress pileup in the soft components of the $E_{\mathrm{T}}^{\mathrm{miss}}$ [38].

5 Event selection

After the application of beam, detector, and data-quality requirements, the total luminosity considered corresponds to $\int L\,\mathrm{d}t = 12.8\ \mathrm{fb}^{-1}$. Events are selected using a trigger based on an $E_{\mathrm{T}}^{\mathrm{miss}}$ selection, which is found to be 99% efficient for events with $E_{\mathrm{T}}^{\mathrm{miss}}$ above 150 GeV. The trigger efficiency variations over data-taking periods or the pileup conditions are measured to be less than 1% after the above requirements. For the 1- and 2-lepton control regions, events are required to pass the unprescaled single lepton trigger with lowest available threshold. A selection $p_{\mathrm{T}} > 25$ GeV is applied to both electrons and muons to ensure the trigger efficiency plateau is reached. The presence of at least one primary vertex (with at least five associated tracks with $p_{\mathrm{T}} > 0.4$ GeV) is required. Jets within $|\eta| < 2.8$ are ordered according to their p_{T}, and it is those jets which are used in the kinematic selections which follow.

A number of event-level variables has been shown to be effective in rejecting the SM background while efficiently selecting candidate sbottom pair production events. The definition of this variables is summarised in Appendix A.

Three sets of signal regions are defined to provide sensitivity to the different kinematic topologies associated to differing mass-splittings Δm between the sbottom and the neutralino mass.

Signal region 1 (SR1) targets signal events with large Δm, identifying the two leading jets as the sbottom decay products. These two leading jets are required to be b-tagged. Events are rejected if any further central ($|\eta| < 2.8$) jets are found with $p_{\mathrm{T}} > 50$ GeV. The multi-jet background is heavily suppressed by selecting events with large $\Delta\phi_{\mathrm{min}}$ and $E_{\mathrm{T}}^{\mathrm{miss}}/\mathrm{m}_{\mathrm{eff}}$. The final selection is done by applying four different thresholds on the boost-corrected contransverse mass, m_{CT}.

Signal region 2 (SR2) targets signal events with moderate Δm. Due to the softer kinematics in this region, the thresholds on the leading jet p_{T} and on the m_{CT} are relaxed. A final upper cut on the additional hadronic activity in the event, $H_{\mathrm{T},2}$, is applied to reject further $t\bar{t}$ production processes.

Signal region 3 (SR3) is defined to enhance the sensitivity in the low Δm region by explicitly selecting final state events with a high p_{T} jet produced as initial state radiation recoiling against the sbottom pair system. High thresholds on the leading jet and on the missing transverse momentum, which are required to be almost back-to-back in ϕ, are imposed. Two additional soft jets are required to be b-tagged. As for SR1 and SR2, the multi-jet background is suppressed with appropriate selections on $\Delta\phi_{\mathrm{min}}$ and $E_{\mathrm{T}}^{\mathrm{miss}}/\mathrm{m}_{\mathrm{eff}}$. A final upper cut on the additional hadronic activity in the event, $H_{\mathrm{T},3}$, completes the selection for SR3a. A second signal region named SR3b is defined by further increasing the thresholds on the leading jet and $E_{\mathrm{T}}^{\mathrm{miss}}$ to explore signals with larger sbottom masses.

The definitions of all signal regions are summarised in Table 1.

Description	Signal region			
	SR1	SR2	SR3a	SR3b
Trigger	$E_{\mathrm{T}}^{\mathrm{miss}}$ trigger $> 99\%$ efficient for $E_{\mathrm{T}}^{\mathrm{miss}} > 150$ GeV			
Event cleaning	Common to all SR			
Lepton veto	No e/μ with $p_{\mathrm{T}} > 10$ GeV			
$E_{\mathrm{T}}^{\mathrm{miss}}$	> 150 GeV	> 200 GeV	> 150 GeV	> 250 GeV
Leading jet $p_{\mathrm{T}}(j_1)$	> 130 GeV, $\lvert\eta\rvert < 2.8$	> 60 GeV, $\lvert\eta\rvert < 2.8$	> 130 GeV, $\lvert\eta\rvert < 2.8$	> 150 GeV, $\lvert\eta\rvert < 2.8$
Second jet $p_{\mathrm{T}}(j_2)$	> 50 GeV, $\lvert\eta\rvert < 2.8$	> 60 GeV, $\lvert\eta\rvert < 2.8$	> 30 GeV, < 110 GeV, $\lvert\eta\rvert < 2.8$	
Third jet $p_{\mathrm{T}}(j_3)$	veto event if $p_{\mathrm{T}}(j_3) > 50$ GeV, $\lvert\eta\rvert < 2.8$		> 30 GeV, $\lvert\eta\rvert < 2.8$	
$\Delta\phi(E_{\mathrm{T}}^{\mathrm{miss}}, j_1)$	-		> 2.5	
jet b-tagging ($\lvert\eta\rvert < 2.5$)	j_1 and j_2 tagged		j_1 anti-tagged, j_2 and j_3 tagged	
$\Delta\phi_{\mathrm{min}}(n)$	> 0.4 ($n = 2$)		> 0.4 ($n = 3$)	
$E_{\mathrm{T}}^{\mathrm{miss}}/\mathrm{m}_{\mathrm{eff}}(j_1, j_2, j_3)$	> 0.25			
m_{CT}	$> 150, 200, 250, 300$ GeV	> 100 GeV	-	
$H_{\mathrm{T},x}$	-	< 50 GeV, $x = 2$	< 50 GeV, $x = 3$	

Table 1: Summary of the event selection in each signal region. The leading, subleading and 3rd leading jet are referred to as j_1, j_2 and j_3, respectively.

6 Background estimate

The dominant SM background processes in the signal regions are top and W + hf (hf = heavy flavour) production (where a charged lepton is produced but it is not vetoed, either because it is a hadronically decaying τ, or because it is an electron or muon out of acceptance or not reconstructed), $Z(\rightarrow \nu\bar{\nu})$+hf and multi-jet production from QCD processes. The sub-dominant background contribution from di-bosons, $t\bar{t}+W/Z$ and $t\bar{t}+b\bar{b}$ is estimated using MC simulation (referred to as "Others" in the following).

The multi-jet production is estimated with a fully data-driven procedure described in detail in Ref. [39], which consists in smearing the jet response of low-$E_{\mathrm{T}}^{\mathrm{miss}}$ seed events. The Gaussian core of the jet response function is obtained from well reconstructed di-jet events, while the non-Gaussian tails are obtained from three-jet events, where the missing transverse momentum can be unambiguously associated to the mis-measurement of one of the jets.

For SR1, the contributions from top production, Z+hf and W+hf production are estimated simultaneously with a profile likelihood fit to three control regions. For SR2 and SR3 the W+hf contribution is estimated using MC and only two control regions are used for the fit. The single top contribution is added to the $t\bar{t}$ background contribution with a relative normalisation corresponding to that predicted by the MC.

The control regions are defined by explicitly requiring the presence of leptons (electrons or muons) in the final state[2] and other selections kinematically close to those of the corresponding signal regions. A set of same-flavour opposite-sign 2-lepton control regions with di-lepton

[2]This ensures no signal contamination from the signal of interest. Moreover, the further kinematical constraints on the control regions ensure small signal contamination also from other possible SUSY processes.

CR1L_SR1	CR2L_SR1	CR2LDF_SR1
1 tight electron or muon	ee or $\mu\mu$	$e\mu$
$p_{\mathrm{T}}(j_1) > 130$ GeV and $p_{\mathrm{T}}(j_2) > 50$ GeV	$p_{\mathrm{T}}(j_1) > 50$ GeV and $p_{\mathrm{T}}(j_2) > 50$ GeV	$p_{\mathrm{T}}(j_1) > 130$ GeV and $p_{\mathrm{T}}(j_2) > 50$ GeV
Veto event if $p_{\mathrm{T}}(j_3) > 50$ GeV		
$E_{\mathrm{T}}^{\mathrm{miss}} > 100$ GeV	$E_{\mathrm{T}}^{\mathrm{miss}}$ (lepton-corrected) > 100 GeV	$E_{\mathrm{T}}^{\mathrm{miss}} > 100$ GeV
Two reconstructed b-jets (leading jets)		
40 GeV $< m_{\mathrm{T}} < 100$ GeV $m_{\mathrm{CT}} > 150$ GeV	75 GeV $< m_{\ell\ell} < 105$ GeV leading lepton $p_{\mathrm{T}} > 90$ GeV	$m_{\ell\ell} >$50 GeV $m_{\mathrm{CT}} > 75$ GeV

Table 2: Definition of the control regions adopted for SR1.

CR1L_SR2	CR2L_SR2
1 tight electron or muon	ee or $\mu\mu$
$p_{\mathrm{T}}(j_1) > 60$ GeV and $p_{\mathrm{T}}(j_2) > 60$ GeV	$p_{\mathrm{T}}(j_1) > 50$ GeV and $p_{\mathrm{T}}(j_2) > 50$ GeV
Veto event if $p_{\mathrm{T}}(j_3) > 50$ GeV	
$E_{\mathrm{T}}^{\mathrm{miss}} > 120$ GeV	$E_{\mathrm{T}}^{\mathrm{miss}}$ (lepton-corrected)> 100 GeV
Two reconstructed b-jets (leading jets)	
40 GeV $< m_{\mathrm{T}} < 100$ GeV	75 GeV $< m_{ll} < 105$ GeV
—	leading lepton $p_{\mathrm{T}} > 90$ GeV

Table 3: Definition of the control regions adopted for SR2.

CR1L_SR3	CR2L_SR3
1 tight electron or muon	ee or $\mu\mu$
Three reconstructed jets	
$p_{\mathrm{T}}(j_1) > 130$ GeV; $100 > p_{\mathrm{T}}(j_2) > 30$ GeV	$p_{\mathrm{T}}(j_1) > 50$ GeV
$E_{\mathrm{T}}^{\mathrm{miss}} > 120$ GeV	$E_{\mathrm{T}}^{\mathrm{miss}}$ (lepton-corrected)> 100 GeV
j_1 anti-tagged, j_2 and j_3 tagged	
40 GeV $< m_{\mathrm{T}} < 100$ GeV	75 GeV $< m_{ll} < 105$ GeV
—	leading lepton $p_{\mathrm{T}} > 90$ GeV

Table 4: Definition of the control regions adopted for SR3.

invariant mass around the Z mass ($75 < m_{\ell\ell} < 105$ GeV) provides a data sample dominated by Z production. For these control regions, labelled in the following as CR2L_SRX, where X=1,2,3, the p_{T} of the leptons is added vectorially to the $E_{\mathrm{T}}^{\mathrm{miss}}$ to mimic the expected missing transverse momentum spectrum of $Z \to \nu\bar{\nu}$ events. In addition, the p_{T} of the leading lepton is required to be above 90 GeV in order to further enhance the Z production contribution. A different-flavour opposite-sign 2-lepton control region (CR2LDF_SR1) with one electron and one muon in the final state with $m_{e\mu} > 50$ GeV and m_{CT} >75 GeV provides a data sample dominated by top pair production which is used to estimate the top contribution to SR1. The set of control regions with exactly one lepton (e, μ) in the final state and 40 GeV $< m_{\mathrm{T}} <$ 100 GeV provides a data sample largely dominated by top and, to a lesser extent, W production. In the following, they are labelled as CR1L_SRX, where X=1,2,3. To further enhance the W contribution in CR1L_SR1 and CR1L_SR2 a further selection $m_{\mathrm{CT}} > 150$ GeV is applied. CR1L_SR1 is used to estimate the contribution of the W+jets background in SR1, while CR1L_SR2 and CR1L_SR3 are dominated by top pair production and are used to establish its contribution in SR2 and SR3. The exact definition of each of the control regions can be found in Tables 2, 3 and 4. The distribution of the transverse mass m_{T} in the 1-lepton control region (before the upper selection on m_{T}) and of the di-lepton invariant mass $m_{\ell\ell}$ in the 2-lepton control region are shown in Figure 1 (for SR1) and in Figure 2 (for SR3) before the fit. In these figures, Monte Carlo based normalisation from the theoretical cross sections is used.

The extrapolation of the SM background to the signal region is performed with a fit based on the profile likelihood method [40]. The free parameters of the fit are the top, the W+jets and the Z+jets overall normalisation values for SR1, and the top and Z+jets normalisation values for SR2 and SR3. The contributions from all other background processes are fixed at the expected value[3]. Systematic uncertainties are treated as nuisance parameters constrained with Gaussian functions and correlations are taken into account. The likelihood function is built as the product of Poisson probability functions, describing the observed and expected number of events in the control and (when excluding SUSY models) signal regions, and the constraints on the nuisance parameters.

The reliability of the MC extrapolation of the SM background estimation is checked in several validation regions. The first set of validation regions is defined with the same kinematic selection as the control regions but with the requirement of one b-tag only. They are used to verify the stability of the b-tagging selection. A second set of 0-lepton validation regions is defined with an identical selection to the signal regions, but reversing one of the cuts. For SR1 and SR2, a selection on $m_{\mathrm{CT}} < 100$ GeV is required in order to avoid overlap with the corresponding signal regions. In the case of SR3, it is the $H_{\mathrm{T,3}}$ requirement that it is reverted by selecting events above 50 GeV for this quantity. Finally, validation regions with two different flavour leptons in the final state are also used to cross check the normalisation of the top background in SR2 and SR3. Good agreement between the fit results and the number of observed events in the validation regions is found in all cases.

The fit results in the control regions are summarised in Table 5 for SR1. These results were found to be compatible with Monte Carlo predictions before the fit. Similar results have been obtained for the control and validation regions of the other signal regions.

[3]The contribution of fake lepton background to the control regions has been estimated with a matrix method [37, 41] and found to be negligible.

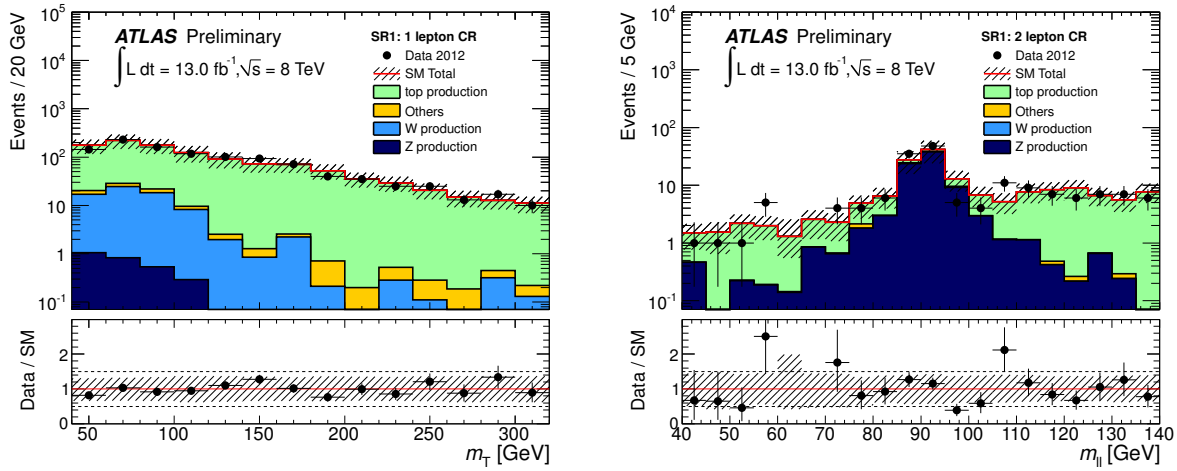

Figure 1: Left: Transverse mass distribution between the lepton and the $E_{\mathrm{T}}^{\mathrm{miss}}$ in CR1L_SR1 (before the m_{T} and m_{CT} selections) for the 1-lepton channel. Right: di-lepton invariant mass distribution in CR2L_SR1 omitting the $m_{\ell\ell}$ cut. The shaded band includes both detector and theoretical systematic uncertainties. The SM prediction is normalised according to the MC expectations.

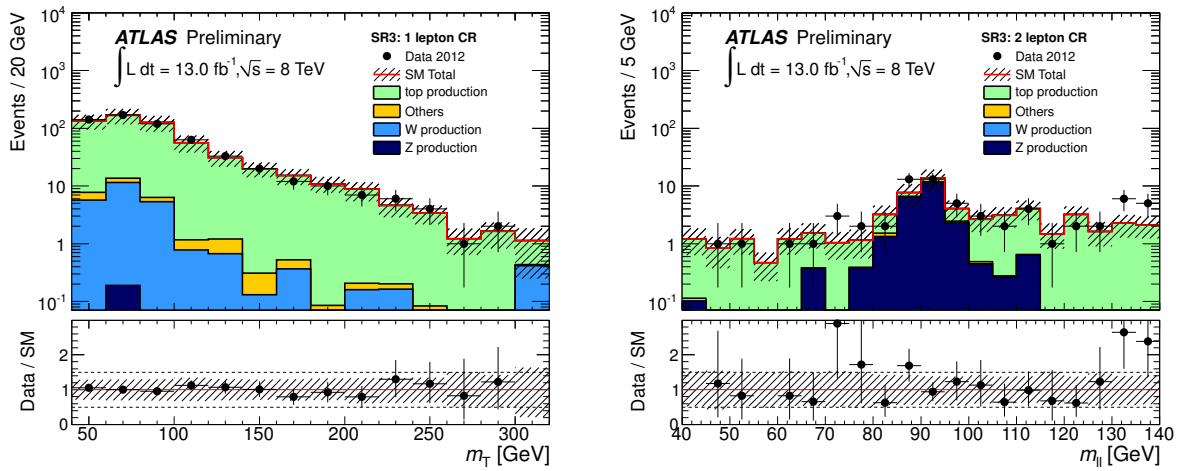

Figure 2: Left: transverse mass distribution between the lepton and the $E_{\mathrm{T}}^{\mathrm{miss}}$ in CR1L_SR3 (before the upper selection on m_{T}) for the 1-lepton channel. Right: di-lepton invariant mass distribution in CR2L_SR3 omitting the $m_{\ell\ell}$ cut. The shaded band includes both detector and theoretical systematic uncertainties. The SM prediction is normalised according to the MC expectations.

Channel	*CR*1*L_SR*1	*CR*2*L_SR*1	*CR*2*LDF_SR*1
Observed events	104	102	51
Fitted bkg events	104 ± 11	102 ± 11	51 ± 7
Top production	70 ± 16	18 ± 4	50 ± 7
Z production	1.5 ± 0.4	82 ± 12	—
W production	25 ± 19	—	—
Others	8 ± 4	2.4 ± 1.3	0.8 ± 0.4

Table 5: Results of the fit for the control regions adopted for SR1. Where no value is given, the background expectation is below 0.1.

7 Systematic uncertainties

The dominant detector-related systematic effects are due to the jet energy scale (JES) and resolution (JER) uncertainties, and the uncertainties on the b-tagging efficiency and mistag rates. The JES uncertainty is derived from a combination of simulations, test beam data and in-situ measurements [35]. Additional terms accounting for flavour composition, flavour response close-by jets, pileup and b-jet uncertainties are taken into account. Uncertainties on the JER are obtained with an in-situ measurement of the jet response asymmetry in di-jet events. These uncertainties on jets are propagated to the $E_{\mathrm{T}}^{\mathrm{miss}}$ measurement, and additional uncertainties on $E_{\mathrm{T}}^{\mathrm{miss}}$ arising from energy deposits not associated with any reconstructed objects are also included. The b-tagging uncertainty is evaluated by varying the η-, p_{T}- and flavour-dependent scale factors applied to each jet in the simulation within a range that reflects the systematic uncertainty on the measured tagging efficiency and mistag rates. The systematic uncertainties in the modelling of the $t\bar{t}$+jets background are assessed as follows: the uncertainty due to the choice of the MC generator is estimated by comparing `POWHEG` to the `MC@NLO` generator [27]; the parton shower (PS) uncertainty is assessed by comparing `POWHEG` interfaced to `PYTHIA` to `POWHEG` interfaced to `HERWIG` and `JIMMY`; the uncertainty due the initial (ISR) and final (FSR) state radiation is estimated by comparing `AcerMC` [25] MC samples generated with different amounts of ISF/FSR. Uncertainties on the W/Z+jets simulation are evaluated by comparing the Sherpa generator with samples generated using the `ALPGEN` MC and by varying the `Sherpa` scales related to the matching scheme, the strong coupling constant, the renormalisation and the factorisation. An uncertainty of 100% is derived for the multi-jet prediction from studying a variation of the resolution function. Finally uncertainties of 30% and of 50% for the cross-section of $t\bar{t}+W$ and of $t\bar{t}+Z$ production, respectively, are assigned [42, 43].

8 Results and interpretation

The number of data events observed in the each signal region is reported in Table 6, together with the SM background expectation after the fit. Figure 3 shows the comparison between the SM prediction and the observed data for several relevant kinematic distributions in the different signal regions. A SUSY sample with a relevant value of Δm between sbottom and neutralino masses is shown for reference for each signal region.

No excess above the SM expectations is observed in any of the signal regions defined. Results are used to obtain model-independent upper limits (UL) on the number of expected beyond SM (BSM) signal events on each signal region, and on the corresponding cross-section,

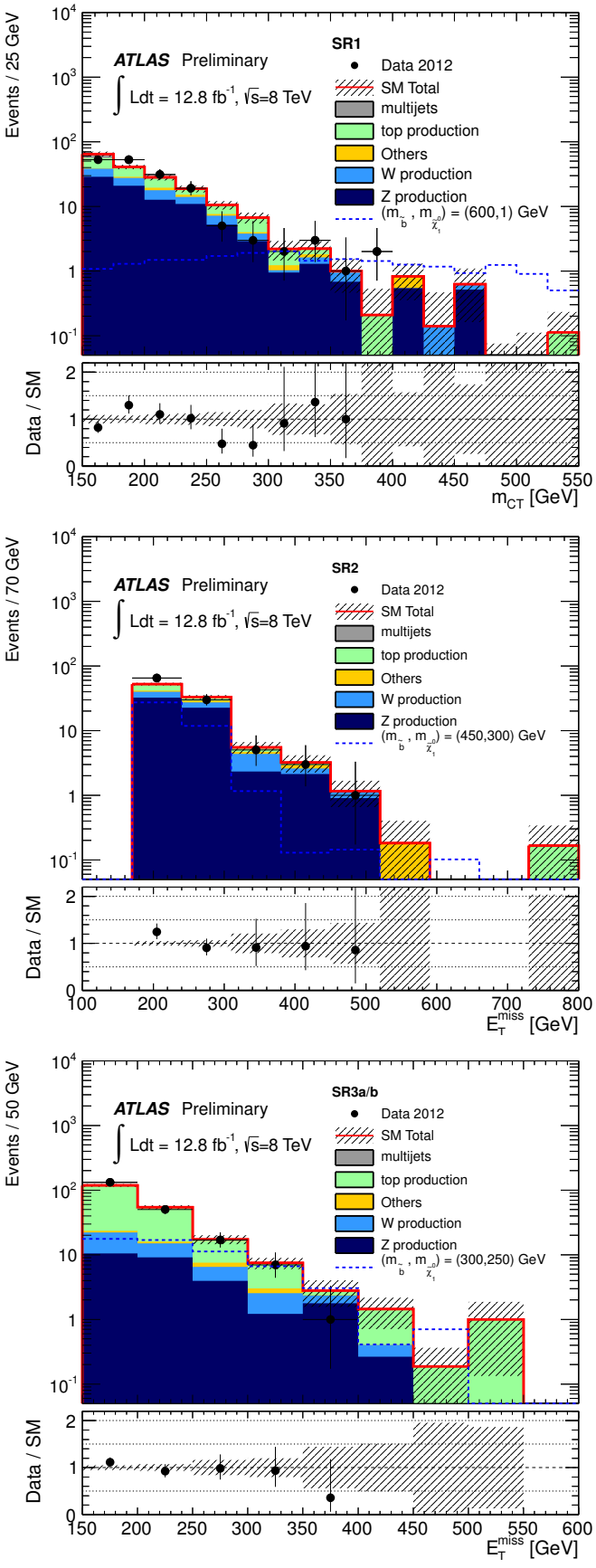

Figure 3: Top: m_{CT} distribution in SR1 before the selection on m_{CT}. Middle: $E_{\mathrm{T}}^{\mathrm{miss}}$ distribution in SR2. Bottom: $E_{\mathrm{T}}^{\mathrm{miss}}$ distribution in SR3 (assuming $p_{\mathrm{T}}(j_1) > 130$ GeV). The shaded band includes both detector and theoretical systematic uncertainties. The backgrounds are normalised to the values determined in the fit.

Channel	SR1, m_{CT} selection				SR2	SR3	
	150 GeV	200 GeV	250 GeV	300 GeV		SR3a	SR3b
Observed	**172**	**66**	**16**	**8**	**104**	**207**	**21**
SM Total	176 ± 25	71 ± 11	25 ± 4	7.4 ± 1.7	95 ± 11	203 ± 35	27 ± 5
Top production	45 ± 13	17 ± 6	7 ± 3	1.6 ± 0.6	15 ± 4	146 ± 40	15 ± 5
Z production	85 ± 15	36 ± 6	12 ± 2	4.0 ± 0.9	60 ± 9	27 ± 9	7 ± 2
W production	28 ± 23	12 ± 10	4 ± 3	1 ± 1	15 ± 5	22 ± 7	4 ± 1
Others	6 ± 3	4 ± 2	1.4 ± 0.8	0.7 ± 0.4	4 ± 2	4 ± 2	1.5 ± 0.9
Multijet production	12 ± 12	2 ± 2	0.2 ± 0.2	0.01 ± 0.01	0.6 ± 0.6	4 ± 4	—

Table 6: For each signal region, the observed event yield is compared with the prediction obtained from the fit. Uncertainties include statistical and systematic uncertainties together.

Signal region	Bkg. estimate	Obs. data	95% CL UL on BSM event yield		95% CL UL on σ_{vis} (fb)	
			expected	observed	expected	observed
SR1 ($m_{CT} > 150$ GeV)	176 ± 25	172	55	54	4.2	4.1
SR1 ($m_{CT} > 200$ GeV)	71 ± 11	66	25	22	1.9	1.7
SR1 ($m_{CT} > 250$ GeV)	25 ± 4	16	12.5	7.9	0.96	0.61
SR1 ($m_{CT} > 300$ GeV)	7.4 ± 1.7	8	7.5	8.0	0.58	0.62
SR2	95 ± 11	104	32	39	2.5	3.0
SR3a	203 ± 35	207	54	54	4.2	4.2
SR3b	27 ± 5	21	13.1	9.6	1.0	0.74

Table 7: Expected and observed event yields with the corresponding Upper Limits (UL) on a generic BSM signal yields and $\sigma_{vis} = \sigma \cdot A \cdot \varepsilon$ for all the signal regions defined.

σ_{vis}, defined as

$$\sigma_{vis} = \sigma \cdot A \cdot \varepsilon \tag{1}$$

where σ, A and ε are, respectively, the production cross-section, the acceptance and the selection efficiency for a generic BSM signal. The *CLs* prescription is used to obtain 95% C.L. limits [40]. Table 7 summarises, for each signal region, the estimated SM background yield, the observed number of events, and the expected and observed UL on event yields from a BSM signal and on σ_{vis}.

Results are interpreted in a specific SUSY scenario which assumes a SUSY particle mass hierarchy such that the sbottom decays exclusively via $\tilde{b}_1 \to b\tilde{\chi}_1^0$. Systematic uncertainties on the signal include experimental uncertainties, mostly dominated by b-tagging ($\sim 28\%$ in SR1 and SR2; $\sim 20\%$ in SR3) and JES ($\sim 1-6\%$ in SR1 and SR2; $\sim 4-30\%$ in SR3, larger when approaching the diagonal) uncertainties. They are assumed to be fully correlated with those of the background. Signal cross sections are calculated to next-to-leading order in the strong coupling constant, adding the resummation of soft gluon emission at next-to-leading-logarithmic accuracy (NLO+NLL) [44–46]. The nominal cross section and the uncertainty are taken from an envelope of cross section predictions using different PDF sets and factorisation and renormalisation scales, as described in Ref. [47].

Figure 4 shows the exclusion limit obtained by taking in each point the signal region with the best expected exclusion. For the MSSM scenario considered, sbottom masses up to 620 GeV

are excluded at 95% C.L. for $m_{\tilde{\chi}_1^0} < 150$ GeV. Neutralino masses up to 320 GeV are excluded for sbottom masses around 550 GeV. Sensitivity to scenarios with large Δm (> 200 GeV) is mostly obtained using the SR1 selections and, to a lesser extent SR2. The best sensitivity in the region Δm <40 GeV for sbottom masses below 300 GeV is obtained with the SR3 selection.

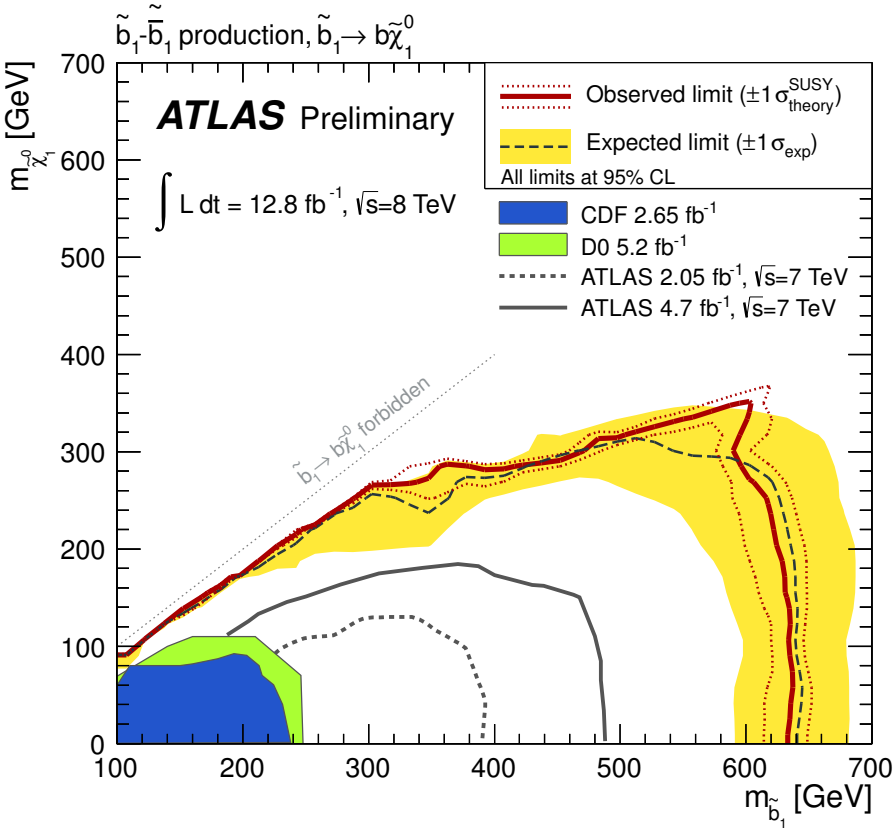

Figure 4: Expected and observed exclusion limits at 95% C.L. in the $(m_{\tilde{b}_1}, m_{\tilde{\chi}_1^0})$ plane obtained taking in each point the signal region which gives the best expected *CLs* exclusion. The black, dashed line shows the expected limit if theory uncertainties on the signal are neglected. The yellow band shows the ± 1 σ Gaussian equivalent uncertainty on the expected limit. The red solid line shows the nominal observed limit, while the red dashed lines show its variation if theory uncertainties on the signal are taken into account. Previous limits set by the ATLAS [19, 20], CDF [48] and D0 [49] are also shown.

9 Conclusions

In summary, we report results of a search for sbottom pair production in pp collisions at $\sqrt{s} =$ 8 TeV, based on 12.8 fb^{-1}of ATLAS data. The events are selected with large $E_{\mathrm{T}}^{\mathrm{miss}}$ and two jets required to originate from b-quarks. The results are in agreement with SM predictions for backgrounds and translate into 95% C.L. upper limits on sbottom and neutralino masses in a given MSSM scenario for which the exclusive decay $\tilde{b}_1 \to b\tilde{\chi}_1^0$ is assumed. Sbottom masses up to 620 GeV are excluded for $m_{\tilde{\chi}_1^0} = 0$. Differences in mass above 40 GeV between the $\tilde{b}_1$ and the $\tilde{\chi}_1^0$ are excluded up to sbottom masses of 300 GeV. Neutralino masses up to 320 GeV are

excluded for sbottom masses around 550 GeV. These limits significantly extending previous results.

A Variable definitions

The following variables have been proven to be useful to reject the SM background effectively. In a given event:

$\Delta\phi_{\rm min}(n)$: This is defined as the minimum $\Delta\phi$ between any of the leading n jets and the $\mathbf{p}_{\rm T}^{\rm miss}$.

$$\Delta\phi_{\rm min} = \min(|\phi_1 - \phi_{\mathbf{p}_{\rm T}^{\rm miss}}|, ..., |\phi_n - \phi_{\mathbf{p}_{\rm T}^{\rm miss}}|) \tag{2}$$

Multi-jet events are predominantly characterised by small values of $\Delta\phi_{\rm min}$.

$\rm m_{eff}$: This is defined as the scalar sum of the $p_{\rm T}$ of the n jets with $p_{\rm T} > 20$ GeV and $|\eta| < 2.8$ and the $E_{\rm T}^{\rm miss}$.

$$\rm m_{eff} = \sum_{i \leq n} (p_{\rm T}^{\rm jet})_i + E_{\rm T}^{\rm miss} \tag{3}$$

where the index refers to the $p_{\rm T}$ ordered list of jets.

$H_{{\rm T},x}$: This is the scalar sum of the $p_{\rm T}$ of the n jets with $p_{\rm T} > 20$ GeV and $|\eta| < 2.8$, without including the leading x jets:

$$H_{{\rm T},x} = \sum_{i=x+1}^{n} (p_{\rm T}^{\rm jet})_i. \tag{4}$$

The number of leading jets x excluded from this sum depends on the signal region under study.

$m_{\rm T}$: This is defined using the transverse momentum of the charged lepton in the event ($\mathbf{p}_{\rm T}^{\rm lep}$) and the $\mathbf{p}_{\rm T}^{\rm miss}$ as follows:

$$m_{\rm T} = \sqrt{2 p_{\rm T}^{\rm lep} E_{\rm T}^{\rm miss} - 2\mathbf{p}_{\rm T}^{\rm lep} \cdot \mathbf{p}_{\rm T}^{\rm miss}} \tag{5}$$

This variable is used in the 1-lepton control region.

$m_{\rm CT}$: The contransverse mass, $m_{\rm CT}$ [50], is a kinematic variable that can be used to measure the masses of pair-produced semi-invisibly decaying heavy particles. For two identical decays of heavy particles into two visible particles (or particle aggregates) v_1 and v_2, and into invisible particles, $m_{\rm CT}$ is defined as:

$$m_{\rm CT}^2(v_1, v_2) = [E_{\rm T}(v_1) + E_{\rm T}(v_2)]^2 - [\mathbf{p}_{\rm T}(v_1) - \mathbf{p}_{\rm T}(v_2)]^2, \tag{6}$$

where $E_{\rm T} = \sqrt{p_{\rm T}^2 + m^2}$. It is an invariant under equal and opposite boosts of the parent particles in the transverse plane. For parent particles produced with small transverse boosts, $m_{\rm CT}$ is bounded from above by an analytical combination of particle masses. This bound is saturated when the two visible objects are co-linear and for the signal under consideration is given by:

$$m_{\rm CT}^{\rm max} = \frac{m^2(\tilde{b}) - m^2(\tilde{\chi}_1^0)}{m(\tilde{b})} \tag{7}$$

The boost-corrected contransverse mass [51] conservatively corrects rudimentary m_{CT} to account for boosts in the transverse plane due to ISR that break the invariance of the quantity. This correction ensures that the calculated m_{CT} is not smeared to higher values due to the boost from ISR and hence protects the expected endpoint in the distribution.

B Auxiliary material

This are additional tables and plots for which we request approval:

Selection	$(m_{\tilde{b}_1}, m_{\tilde{\chi}_1^0}) = (300, 250)$ GeV	$(m_{\tilde{b}_1}, m_{\tilde{\chi}_1^0}) = (450, 300)$ GeV	$(m_{\tilde{b}_1}, m_{\tilde{\chi}_1^0}) = (600, 1)$ GeV
$E_{\mathrm{T}}^{\mathrm{miss}}$	3.5e+03	1.1e+03	2.7e+02
Jet multipl.	3.5e+03	1e+03	2.6e+02
j_1	2.4e+03	7.6e+02	2.6e+02
j_2	1.9e+03	6.7e+02	2.5e+02
j_3 veto	8.6e+02	3.1e+02	1.1e+02
$\Delta\phi_{\mathrm{min}}(3)$	6.6e+02	2.8e+02	93
$E_{\mathrm{T}}^{\mathrm{miss}}/\mathrm{m}_{\mathrm{eff}}(j_1, j_2, j_3)$	6.6e+02	2.7e+02	84
jet b-tagging	9.9	84	24
$m_{\mathrm{CT}} > 100$	4.3	79	23
$m_{\mathrm{CT}} > 150$	2.5	58	22
$m_{\mathrm{CT}} > 200$	0.9	21	19
$m_{\mathrm{CT}} > 250$	0.33	1.3	16
$m_{\mathrm{CT}} > 300$	0	0	13

Table 8: Breakdown of SR1 event selection for three different signal points with different mass differences between the $\tilde{b}_1$and the $\tilde{\chi}_1^0$. Numbers are normalised assuming 12.8 fb^{-1}.

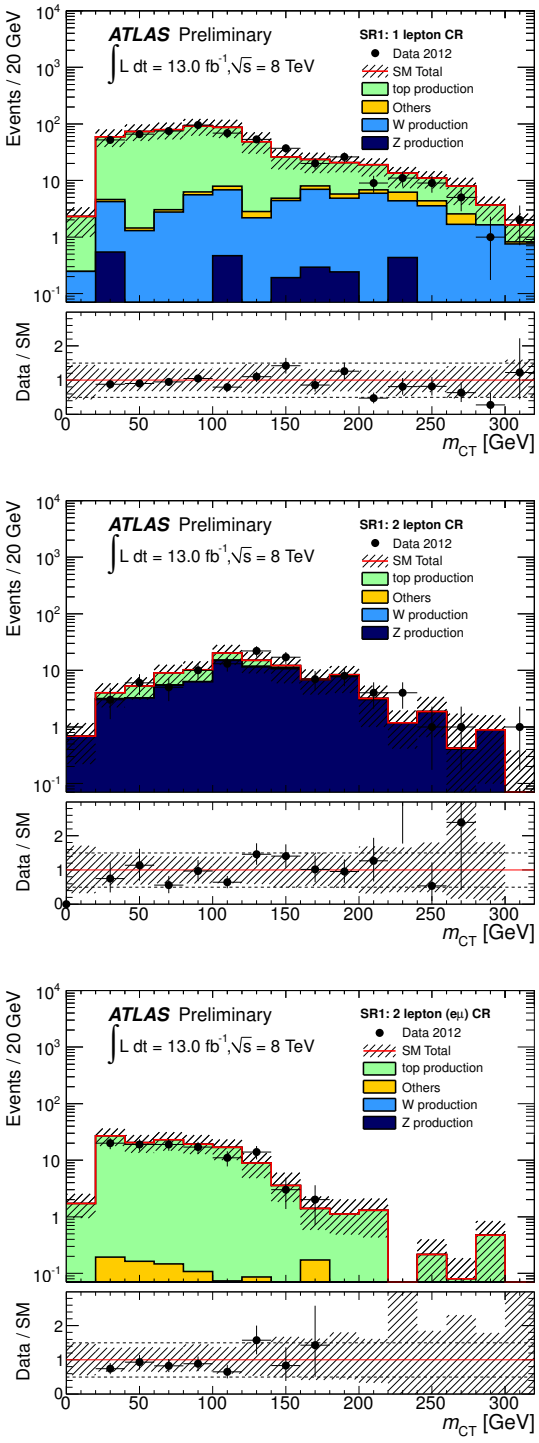

Figure 5: Distributions of m_{CT} for the control regions adopted for SR1. Top: the single-lepton control region. Middle: the di-leptonic (Z-enhanced) control region. Bottom: the di-leptonic different-flavour control region. The shaded band includes both detector and theoretical systematic uncertainties. The SM prediction is normalised according to the MC expectations. For the top and bottom plots, the final selection on m_{CT} has been omitted.

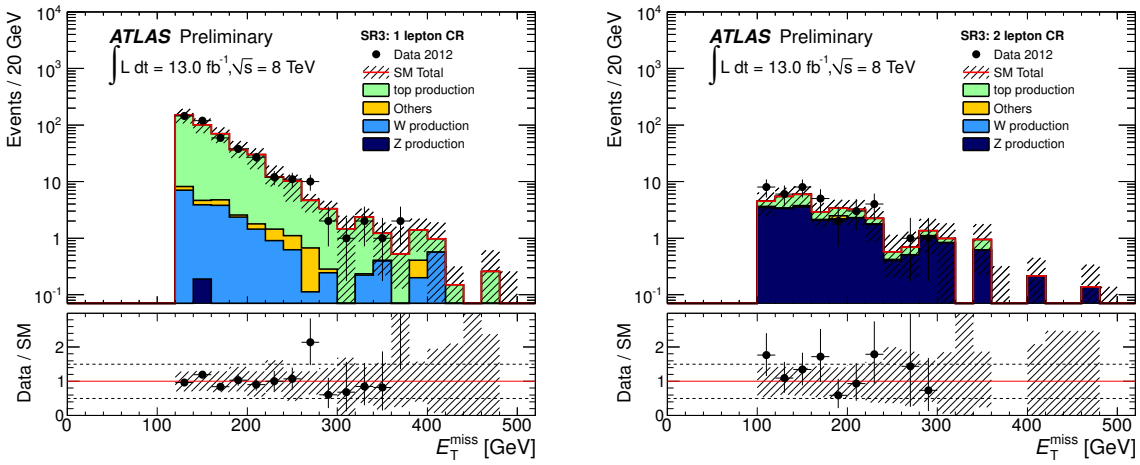

Figure 6: Distribution of $E_{\mathrm{T}}^{\mathrm{miss}}$ in the (left) single-lepton (right) di-leptonic (Z-enhanced) control region adopted for SR3. The shaded band includes both detector and theoretical systematic uncertainties. The SM prediction is normalised according to the MC expectations.

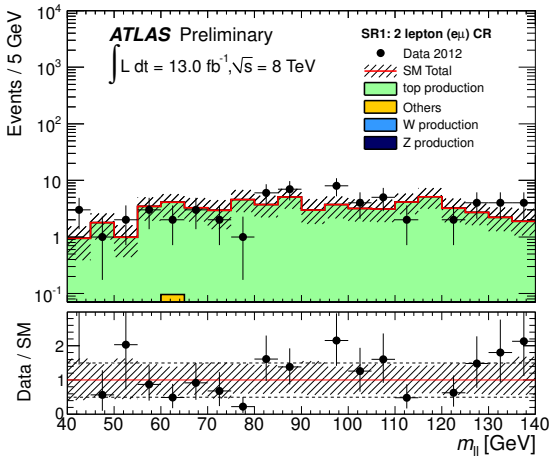

Figure 7: Distribution of $m_{e\mu}$ distribution in the di-leptonic different-flavour control region adopted for SR1. The shaded band includes both detector and theoretical systematic uncertainties. The SM prediction is normalised according to the MC expectations.

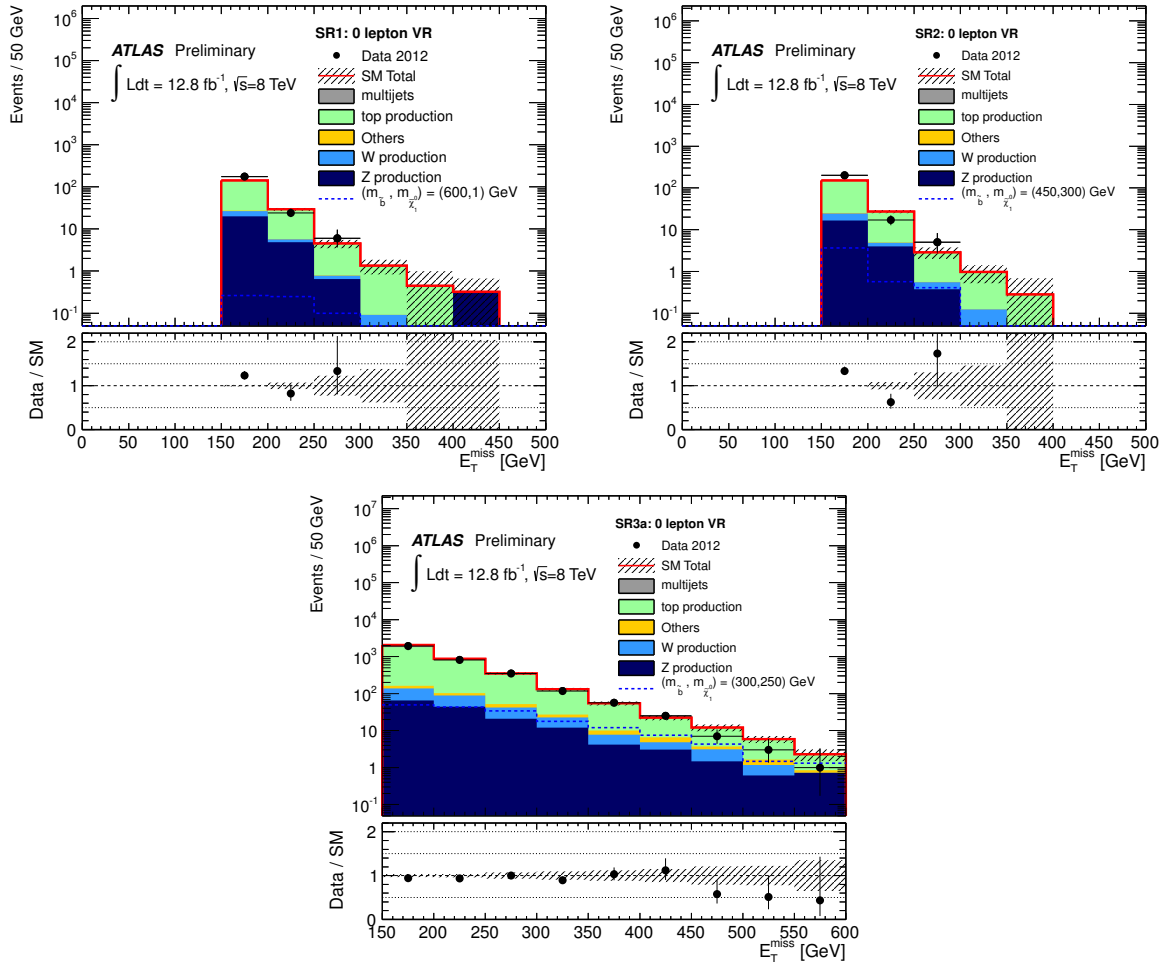

Figure 8: Distributions of $E_{\mathrm{T}}^{\mathrm{miss}}$in the different no lepton validation regions for each of the signal regions, as discussed in the text. The shaded band includes both detector and theoretical systematic uncertainties. The backgrounds are normalised to the values determined in the fit.

Selection	$(m_{\tilde{b}_1}, m_{\tilde{\chi}_1^0}) = (300, 250)$ GeV	$(m_{\tilde{b}_1}, m_{\tilde{\chi}_1^0}) = (450, 300)$ GeV	$(m_{\tilde{b}_1}, m_{\tilde{\chi}_1^0}) = (600, 1)$ GeV
$E_{\mathrm{T}}^{\mathrm{miss}} > 150$ GeV	3.5e+03	1.1e+03	2.7e+02
Jet multipl.	3.5e+03	1e+03	2.6e+02
j_1	3.4e+03	1e+03	2.6e+02
j_2	2.1e+03	8.3e+02	2.5e+02
j_3 veto	8.9e+02	3.9e+02	1e+02
$\Delta\phi_{\mathrm{min}}(3)$	7.2e+02	3.6e+02	91
$E_{\mathrm{T}}^{\mathrm{miss}}/\mathrm{m}_{\mathrm{eff}}(j_1, j_2, j_3)$	7.2e+02	3.6e+02	82
jet b-tagging	11	1.1e+02	24
$H_{\mathrm{T},2}$	3.3	79	15
$m_{\mathrm{CT}} > 100$	0.84	76	15
$E_{\mathrm{T}}^{\mathrm{miss}} > 200$ GeV	0.27	41	14

Table 9: Breakdown of SR2 event selection for three different signal points with different mass differences between the $\tilde{b}_1$and the $\tilde{\chi}_1^0$. Numbers are normalised assuming 12.8 fb^{-1}.

Selection	$(m_{\tilde{b}_1}, m_{\tilde{\chi}_1^0}) = (300, 250)$ GeV	$(m_{\tilde{b}_1}, m_{\tilde{\chi}_1^0}) = (450, 300)$ GeV	$(m_{\tilde{b}_1}, m_{\tilde{\chi}_1^0}) = (600, 1)$ GeV
j_1	3.4e+03	1e+03	2.8e+02
Jet multipl.	3.1e+03	8.8e+02	2.5e+02
j_2	3e+03	8.6e+02	2.5e+02
j_3	2.5e+03	6.9e+02	2.1e+02
$E_{\mathrm{T}}^{\mathrm{miss}} > 150$ GeV	1.8e+03	5.2e+02	1.9e+02
$\Delta\phi_{\mathrm{min}}(3)$	1.4e+03	4.5e+02	1.7e+02
$E_{\mathrm{T}}^{\mathrm{miss}}/\mathrm{m}_{\mathrm{eff}}(j_1, j_2, j_3)$	1.4e+03	4.3e+02	1.5e+02
j_1 anti-tagged	1.3e+03	2.6e+02	76
jet b-tagging	1.1e+02	37	5.1
$p_{\mathrm{T}}(j_2) < 110$ GeV	90	13	0.39
$H_{\mathrm{T},3}$	58	6.9	0.032
$E_{\mathrm{T}}^{\mathrm{miss}} > 250$ GeV	23	4.3	0.024
$p_{\mathrm{T}}(j_1) > 150$ GeV	23	3.7	0.024

Table 10: Breakdown of SR3 event selections for three different signal points with different mass differences between the $\tilde{b}_1$ and the $\tilde{\chi}_1^0$. Numbers are normalised assuming 12.8 fb^{-1}.

References

[1] H. Miyazawa, *Baryon Number Changing Currents*, Prog. Theor. Phys. **36 (6)** (1966) 1266–1276.

[2] P. Ramond, *Dual Theory for Free Fermions*, Phys. Rev. **D3** (1971) 2415–2418.

[3] Y. A. Gol'fand and E. P. Likhtman, *Extension of the Algebra of Poincare Group Generators and Violation of p Invariance*, JETP Lett. **13** (1971) 323–326. [Pisma Zh.Eksp.Teor.Fiz.13:452-455,1971].

[4] A. Neveu and J. H. Schwarz, *Factorizable dual model of pions*, Nucl. Phys. **B31** (1971) 86–112.

[5] A. Neveu and J. H. Schwarz, *Quark Model of Dual Pions*, Phys. Rev. **D4** (1971) 1109–1111.

[6] J. Gervais and B. Sakita, *Field theory interpretation of supergauges in dual models*, Nucl. Phys. **B34** (1971) 632–639.

[7] D. V. Volkov and V. P. Akulov, *Is the Neutrino a Goldstone Particle?*, Phys. Lett. **B46** (1973) 109–110.

[8] J. Wess and B. Zumino, *A Lagrangian Model Invariant Under Supergauge Transformations*, Phys. Lett. **B49** (1974) 52.

[9] J. Wess and B. Zumino, *Supergauge Transformations in Four-Dimensions*, Nucl. Phys. **B70** (1974) 39–50.

[10] S. Weinberg, *Implications of Dynamical Symmetry Breaking*, Phys. Rev. **D13** (1976) 974–996.

[11] E. Gildener, *Gauge Symmetry Hierarchies*, Phys. Rev. **D14** (1976) 1667.

[12] S. Weinberg, *Implications of Dynamical Symmetry Breaking: An Addendum*, Phys. Rev. **D19** (1979) 1277–1280.

[13] L. Susskind, *Dynamics of Spontaneous Symmetry Breaking in the Weinberg- Salam Theory*, Phys. Rev. **D20** (1979) 2619–2625.

[14] P. Fayet, *Supersymmetry and Weak, Electromagnetic and Strong Interactions*, Phys. Lett. **B64** (1976) 159.

[15] P. Fayet, *Spontaneously Broken Supersymmetric Theories of Weak, Electromagnetic and Strong Interactions*, Phys. Lett. **B69** (1977) 489.

[16] G. R. Farrar and P. Fayet, *Phenomenology of the Production, Decay, and Detection of New Hadronic States Associated with Supersymmetry*, Phys. Lett. **B76** (1978) 575–579.

[17] P. Fayet, *Relations Between the Masses of the Superpartners of Leptons and Quarks, the Goldstino Couplings and the Neutral Currents*, Phys. Lett. **B84** (1979) 416.

[18] S. Dimopoulos and H. Georgi, *Softly Broken Supersymmetry and SU(5)*, Nucl. Phys. **B193** (1981) 150.

[19] ATLAS Collaboration Collaboration, G. Aad et al., *Search for scalar bottom pair production with the ATLAS detector in pp Collisions at* $\sqrt{s} = 7$ *TeV*, Phys. Rev. Lett. **108** (2012) 181802, arXiv:1112.3832 [hep-ex].

[20] ATLAS Collaboration, *Search for scalar bottom pair production in nal states with missing transverse momentum and two b-jets in pp collisions at s=7 TeV with the ATLAS Detector*, ATLAS-CONF-2012-106, 2012.

[21] ATLAS Collaboration, *The ATLAS Experiment at the CERN Large Hadron Collider*, JINST **3** (2008) S08003.

[22] S. Frixione and others, *Matching NLO QCD computations with parton showers simulations: the POWHEG method*, JHEP **11** (2007) 070.

[23] T. Sjöstrand, S. Mrenna, and P. Skands, *PYTHIA 6.4 physics and manual*, JHEP **05** (2006) 026.

[24] H.-L. Lai, M. Guzzi, J. Huston, Z. Li, P. M. Nadolsky, et al., *New parton distributions for collider physics*, Phys. Rev. **D82** (2010) 074024, arXiv:1007.2241 [hep-ph].

[25] B. P. Kersevan and E. Richter-Was, *The Monte Carlo event generator AcerMC version 2.0 with interfaces to PYTHIA 6.2 and HERWIG 6.5*, arXiv:hep-ph/0405247.

[26] J. Pumplin et al., *New generation of parton distributions with uncertainties from global QCD analysis*, JHEP **07** (2002) 012.

[27] S. Frixione and B. R. Webber, *The MC@NLO 3.2 event generator*, arXiv:hep-ph/0601192 [hep-ph].

[28] G. Corcella et al., *HERWIG 6: An Event generator for hadron emission reactions with interfering gluons (including supersymmetric processes)*, JHEP **0101** (2001) 010, arXiv:hep-ph/0011363 [hep-ph].

[29] J. Butterworth, J. Forshaw, and M. Seymour, *Multiparton interactions in photoproduction at HERA*, ZPC **72** (1996) 637–646.

[30] T. Gleisberg, S. Hoeche, F. Krauss, M. Schonherr, S. Schumann, et al., *Event generation with SHERPA 1.1*, JHEP **0902** (2009) 007, arXiv:0811.4622 [hep-ph].

[31] M. Bahr, S. Gieseke, M. Gigg, D. Grellscheid, K. Hamilton, et al., *Herwig++ Physics and Manual*, Eur. Phys. J. **C58** (2008) 639–707, arXiv:0803.0883 [hep-ph].

[32] ATLAS Collaboration, *The ATLAS Simulation Infrastructure*, Eur. Phys. J. **C70** (2010) 823–874, arXiv:1005.4568 [physics.ins-det].

[33] M. Cacciari, G. Salam, and G. Soyez, *The anti-k_t jet clustering algorithm*, JHEP **04** (2008) 063, arXiv:0802.1189 [hep-ph].

[34] M. Cacciari and G. P. Salam, *Dispelling the N^3 myth for the k_t jet-finder*, Phys. Lett. **B641** (2006) 57–61, arXiv:hep-ph/0512210 [hep-ph].

[35] ATLAS Collaboration Collaboration, G. Aad et al., *Jet energy measurement with the ATLAS detector in proton-proton collisions at $\sqrt{s} = 7$ TeV*, arXiv:1112.6426 [hep-ex].

[36] ATLAS Collaboration, *Measurement of the b-tag Efficiency in a Sample of Jets Containing Muons with 5 fb^{-1} of Data from the ATLAS Detector*, ATLAS-CONF-2012-043, 2012.

[37] ATLAS Collaboration Collaboration, G. Aad et al., *Electron performance measurements with the ATLAS detector using the 2010 LHC proton-proton collision data*, Eur. Phys. J. **C72** (2012) 1909, arXiv:1110.3174 [hep-ex].

[38] ATLAS Collaboration, *Performance of Missing Transverse Momentum Reconstruction in ATLAS with 2011 Proton-Proton Collisions at $\sqrt{s}$=7 TeV*, ATLAS-CONF-2012-101, 2012.

[39] ATLAS Collaboration Collaboration, G. Aad et al., *Search for squarks and gluinos with the ATLAS detector in final states with jets and missing transverse momentum using 4.7 fb^{-1} of $\sqrt{s} = 7$ TeV proton-proton collision data*, arXiv:1208.0949 [hep-ex].

[40] G. Cowan, K. Cranmer, E. Gross, and O. Vitells, *Asymptotic formulae for likelihood-based tests of new physics*, Eur. Phys. J. **C71** (2011) 1–19, arXiv:1007.1727 [physics.data-an].

[41] ATLAS Collaboration, *Searches for supersymmetry with the ATLAS detector using final states with two leptons and missing transverse momentum in sqrts = 7 TeV proton-proton collisions*, Phys. Lett. **B709** (2012) 137–157, arXiv:1110.6189 [hep-ex].

[42] M. Garzelli, A. Kardos, C. Papadopoulos, and Z. Trocsanyi, *t tbar W and t tbar Z Hadroproduction at NLO accuracy in QCD with Parton Shower and Hadronization effects*, arXiv:1208.2665 [hep-ph].

[43] J. M. Campbell and R. K. Ellis, *$t\bar{t}W^{+-}$ production and decay at NLO*, JHEP **1207** (2012) 052, arXiv:1204.5678 [hep-ph].

[44] W. Beenakker, M. Kramer, T. Plehn, M. Spira, and P. M. Zerwas, *Stop production at hadron colliders*, Nucl. Phys. **B515** (1998) 3–14, hep-ph/9710451.

[45] W. Beenakker, S. Brensing, M. Kramer, A. Kulesza, E. Laenen, and I. Niessen, *Supersymmetric top and bottom squark production at hadron colliders*, JHEP. **1008** (2010) 098, arXiv:1006.4771 [hep-ph].

[46] W. Beenakker, S. Brensing, M. Kramer, A. Kulesza, E. Laenen, et al., *Squark and Gluino Hadroproduction*, Int. J. Mod. Phys. **A26** (2011) 2637–2664, arXiv:1105.1110 [hep-ph].

[47] M. Kramer, A. Kulesza, R. van der Leeuw, M. Mangano, S. Padhi, et al., *Supersymmetry production cross sections in pp collisions at $\sqrt{s} = 7$ TeV*, arXiv:1206.2892 [hep-ph].

[48] CDF Collaboration Collaboration, T. Aaltonen et al., *Search for the Production of Scalar Bottom Quarks in $p\bar{p}$ collisions at $\sqrt{s}$ = 1.96 TeV*, Phys. Rev. Lett. **105** (2010) 081802, arXiv:1005.3600 [hep-ex].

[49] D0 Collaboration Collaboration, V. M. Abazov et al., *Search for scalar bottom quarks and third-generation leptoquarks in pp^- bar collisions at $\sqrt{s} = 1.96$ TeV*, Phys. Lett. **B693** (2010) 95–101, arXiv:1005.2222 [hep-ex].

[50] D. Tovey, *On measuring the masses of pair-produced semi-invisibly decaying particles at hadron colliders*, JHEP **04** (2008) 034, arXiv:0802.2879 [hep-ph].

[51] G. Polesello and D. Tovey, *Supersymmetric particle mass measurement with the boost-corrected contransverse mass*, JHEP **03** (2010) 030, arXiv:0910.0174 [hep-ph].